

A NEW 24 μm PHASE CURVE FOR v ANDROMEDAE b

IAN J. CROSSFIELD¹, BRAD M. S. HANSEN^{1,2}, JOSEPH HARRINGTON³, JAMES Y-K. CHO⁴, DRAKE DEMING⁵, KRISTEN MENOU⁶, SARA SEAGER⁷

Submitted to ApJ 2010 August 2.

ABSTRACT

We report the detection of 24 μm variations from the planet-hosting v Andromedae system consistent with the orbital periodicity of the system’s innermost planet, v And b. We find a peak-to-valley phase curve amplitude of 0.00130 times the mean system flux. Using a simple model with two hemispheres of constant surface brightness and assuming a planetary radius of 1.3 R_J gives a planetary temperature contrast of $\gtrsim 900$ K and an orbital inclination of $\gtrsim 28^\circ$. We further report the largest phase offset yet observed for an extrasolar planet: the flux maximum occurs $\sim 80^\circ$ before phase 0.5. Such a large phase offset is difficult to reconcile with most current atmospheric circulation models. We improve on earlier observations of this system in several important ways: (1) observations of a flux calibrator star demonstrate the MIPS detector is stable to 10^{-4} on long timescales, (2) we note that the background light varies systematically due to spacecraft operations, precluding use of this background as a flux calibrator (stellar flux measured above the background is not similarly affected), and (3) we calibrate for flux variability correlated with motion of the star on the MIPS detector. A reanalysis of our earlier observations of this system is consistent with our new result.

Subject headings: infrared: planetary systems — planets and satellites: individual (v And b) — planetary systems — techniques: photometric — stars: individual (v And)

1. INTRODUCTION

The first thermal characterizations of highly irradiated extrasolar planetary atmospheres were made by measuring the flux decrement that occurs during secondary eclipse, when an extrasolar planet passes behind its host star (Deming et al. 2005; Charbonneau et al. 2005). This decrement gives an estimate of the (hemisphere-averaged) temperature of a planet’s star-facing side at the time of eclipse and provides insight into the energy budgets of these hot worlds. Secondary eclipse (or, occultation) observations have been widely interpreted as indicating two types of planetary atmospheres, namely planets with and without high-altitude temperature inversions (Burrows et al. 2008; Fortney et al. 2008). However, the number of free parameters in current models is such that in many cases it is still difficult to place strong constraints on a planet’s atmospheric structure with the few data points available for most systems (Madhusudan & Seager 2009).

Burrows et al. (2008) and Fortney et al. (2008) suggested that sufficiently high levels of irradiation prevent strong optically absorbing species from condensing and “raining out” of the upper atmosphere of hot Jupiters, thus directly linking high levels of incident stellar flux to the presence of a temperature inversion. However, subsequent secondary eclipse measurements with Spitzer/IRAC have complicated the picture and a straightforward connection between irradiation and inversions now seems untenable. For example, TrES-3b receives substantially more flux than does HD 209458b, yet the latter has an atmospheric inversion (Knutson et al. 2008) while the former does not (Fressin et al. 2010). Thus, planetary classification will require more subtlety than a simple critical-flux level model can provide. Knutson et al. (2010) have recently suggested a correlation between stellar activity and the absence of a temperature inversion: in this hypothesis high-altitude absorbing species are photodissociated by the ultraviolet flux from an active star. It remains to be seen how this theory addresses the issue of temporally variable stellar activity (Shkolnik et al. 2008).

Phase curves provide complementary insights into planetary atmospheres. If a system’s total (star plus planet) infrared flux varies periodically and in phase with the planet’s orbit, the variation can be attributed to spatially nonuniform radiation emitted by the planet. Such measurements have the potential to constrain the planet’s circulation and heat redistribution patterns. If incident stellar flux were instantaneously re-radiated by the planet, the hottest region on the planet would be at the substellar point; such a phase curve is said to have zero phase offset. Nonzero phase offsets thus imply heat transport around the planet; for example, by advection of absorbed stellar energy by global winds (Showman et al. 2009), or by heating induced by atmospheric

¹Department of Physics & Astronomy, University of California Los Angeles, Los Angeles, CA 90095, USA; ianc@astro.ucla.edu

²Institute of Geophysics & Planetary Physics, University of California Los Angeles, Los Angeles, CA 90095, USA; hansen@astro.ucla.edu

³Planetary Sciences Group, Department of Physics, University of Central Florida, Orlando, FL 32816-2385, USA; jh@physics.ucf.edu

⁷School of Mathematical Sciences, Queen Mary, University of London, London E1 4NS, UK; J.Cho@qmul.ac.uk

⁴Planetary Systems Branch Code 693, NASA/Goddard Space Flight Center, Greenbelt, MD 20771, USA; Leo.D.Deming@nasa.gov

⁶Department of Astronomy, Columbia University, New York, NY 10027, USA; kristen@astro.columbia.edu

⁵Department of Earth, Atmospheric and Planetary Sciences, Department of Physics, Massachusetts Institute of Technology, Cambridge, MA 02139, USA; seager@mit.edu

gravity waves (Watkins & Cho 2010). Interpreting phase curves can be challenging because the brightest atmospheric region will also depend on the opacity structure of the atmosphere and the wavelength at which one observes the system.

The extrasolar planet v Andromedae b (v And b) is the first exoplanet for which a phase curve was reported. Harrington et al. (2006; hereafter H06) used Spitzer/MIPS to measure the $24\ \mu\text{m}$ system flux at five epochs over one orbit and reported a finite amplitude phase curve consistent with zero phase offset, though here we report a new analysis and interpretation of our H06 data based on a better understanding of MIPS systematics. The $8\ \mu\text{m}$ observations of Cowan et al. (2007) also found variations with zero phase offset for HD 179949b. Observations of the less intensely irradiated planet HD 189733b at $8\ \mu\text{m}$ and $24\ \mu\text{m}$ (Knutson et al. 2007, 2009) revealed a relatively small temperature contrast between the planet’s day and night sides and a $30^\circ - 40^\circ$ phase offset, indicating a moderate level of eastward heat redistribution from the warm dayside to the cool night side. It is important to note a possible observational bias: the first two phase curves were sparsely sampled and are for non-transiting systems with unknown orbital inclinations. Though simulations suggest inclination should not substantially affect a planet’s observed phase offset, the flux amplitude will be directly affected by inclination (Rauscher et al. 2008); furthermore, phase curve interpretations are more ambiguous without the absolute calibration provided by a secondary eclipse (Burrows et al. 2008).

Several groups have hypothesized a connection between temperature inversions and the magnitude of a system’s phase offset (e.g., Burrows et al. 2008; Fortney et al. 2008). The favored (though unproven) cause of inversions is a species residing at high altitude that absorbs optically but is transparent to infrared radiation. In this scenario an inverted atmosphere absorbs stellar energy at lower pressures where it should quickly reradiate to space; in a non-inverted atmosphere the energy is absorbed much deeper, where it may circulate farther around the planet and cause a measurable phase offset. Showman et al. (2009) do a fair job of reproducing the HD 189733b phase curves, but they predict secondary eclipse depths for the more highly irradiated HD 209458b that do not match the observations of Knutson et al. (2008); Burrows et al. (2010) also model HD 209458b and they, too, do not match the observed eclipse depths especially well. Thus, our current understanding of the atmospheric structure and dynamics of even the best-characterized planets still appears to be incomplete.

This is the context in which we obtained the high-cadence $24\ \mu\text{m}$ phase curve of v And b described below. We introduce the v Andromedae system, and discuss our observations and data analysis, in Sec. 2. In Sec. 3 we describe the planetary temperature contrast and heat redistribution implied by our analysis. We discuss possible interpretations of our results in Sec. 4, and conclude in Sec. 5.

2. OBSERVATIONS AND ANALYSIS

2.1. The v Andromedae System

The planet v And b was one of the earliest reported hot Jupiters (Butler et al. 1997), and the three-planet v And system has been observed numerous times in the years since (Butler et al. 2006; Naef et al. 2004; Wittenmyer et al. 2007; McArthur et al. 2010). The host star has a spectroscopic effective temperature of $6212 \pm 64\ \text{K}$ (Santos et al. 2004) and a directly-measured diameter of $1.631 \pm 0.014\ R_\odot$ (Baines et al. 2008). Spectroscopic and isochronal mass estimates generally agree on a mass of $\sim 1.3\ M_\odot$ (Fuhrmann et al. 1998; Ford et al. 1999; Valenti & Fischer 2005; Takeda et al. 2007). Because this system’s planets do not transit we do not know their physical sizes; however, if we assume v And b is a typical hot Jupiter we can estimate its radius to be $\sim 1.3\ R_J$ ⁸.

Using a combination of radial velocity and astrometry McArthur et al. (2010) recently determined the orbits of the second and third planets in the v And system to be mutually inclined by 30° . They suggest this nonplanar system may result from planet-planet scattering that could also have moved the innermost planet, v And b, into its current orbit at 0.059 AU. The small stellar reflex motion induced by v And b precluded a direct measurement of its orbital inclination, but their preliminary numerical simulations extending $10^5\ \text{yr}$ suggest v And b’s inclination may lie in the range $\sim 20\text{--}45^\circ$ (implying a planetary mass of $2\text{--}3\ M_J$). Though their simulations did not fully explore the available parameter space, the inclination range McArthur et al. (2010) suggest for v And b is broadly consistent with the constraints we place on its inclination in Sec. 3.

2.2. Observations

We observed the v And system with Spitzer’s MIPS $24\ \mu\text{m}$ channel (Rieke et al. 2004) with observations spread across 1.2 orbits of v And b (~ 5 days) during February 2009. The observations consist of seven brief (~ 3000 seconds on target) observational epochs and one long, near-continuous observation ~ 28 hours in length and centered at phase 0.5 (secondary eclipse for transiting systems in circular orbits, and the predicted time of flux maximum based on H06). Our integrations total 18.5 hours. Spitzer breaks up observations into blocks of time called astronomical observation requests (AORs) for instrument scheduling purposes: our short observations consist of three sequential AORs, and the long observing sequence consists of 71 AORs. Altogether our data consist of 25 488 frames, each with an integration time of 1.57 seconds. We also observe a flux calibrator star, HD 9712, in three two-AOR epochs, for a total of 1.3 hours of integration. The observations of v And by H06, which we reanalyze, consist of five AORs spaced over ~ 5 days.

2.3. Data Reduction

We use the basic calibrated data (BCD) files generated by version 18.14 of the MIPS data reduction pipeline (Masci et al. 2005). During MIPS observations the instrument and spacecraft dither the target star between fourteen positions on the detector (SSC 2007, Section 8.2.1.2). As noted previously (Deming et al. 2005; H06; Knutson et al. 2009) the MIPS detector response

⁸ Taken from the Extrasolar Planets Encyclopedia at <http://exoplanet.eu>

is spatially nonuniform and so we treat the observations as consisting of fourteen separate time series, modeling their systematics separately in the final fit. In each frame we measure the system flux and the position of the star on the detector by fitting a $100\times$ supersampled model MIPS PSF⁹ generated using a 6200 K blackbody spectrum. We shift and scale the model PSF to determine the best-fitting combination of background, stellar flux, and PSF position. Using position-dependent model PSFs does not significantly change our results, so in all our photometry we use a single model PSF generated at the center of the MIPS field of view. We exclude hot pixels from the PSF fit by setting to zero the weight of any frame’s pixel that is more than 5σ discrepant from the median value of that pixel for all frames taken at that particular dither position, and also exclude bad pixels flagged by the MIPS reduction pipeline.

In each set of ~ 40 frames, the first frame has $\sim 3\%$ higher stellar flux, and the first several frames have a lower background, than the rest of the frames in the set. These effects may be related to the MIPS “first-frame” chip reset effect, though the effect we see is qualitatively different from the one described in the MIPS Instrument Handbook (SSC 2010). We exclude the first frame in each set from the remainder of our analysis, removing 708 frames. We further exclude the first three contiguous AORs (700 frames, ~ 40 minutes), which are markedly discrepant from the final time series. These first data were taken soon after a thermal anneal of the MIPS detector, and during these observations we see anomalous readings in the $24\ \mu\text{m}$ detector anneal current, the scan mirror temperature, and the MIPS B side temperature sensor.

The initial extracted photometry reveals a clear sinusoidal flux variation, but with additional variability correlated with the subpixel motion of the star on the detector, as shown in Figures 1 and 2. This effect is likely from imperfect flat fielding rather than an intrapixel sensitivity variation as seen in the Infrared Array Camera’s 3.6 and $4.5\ \mu\text{m}$ channels (Reach et al. 2005; Charbonneau et al. 2005), because several time series with similar intrapixel locations exhibit anticorrelated flux variations. We tried creating a flat field by median-stacking all the BCD frames after masking the region containing the target star, but applying this flat field to the data before computing photometry did not reduce the amplitude of the position-correlated photometric variability. As we describe below, we suspect intermittent, low levels of scattered light interfere with our ability to construct a sufficiently accurate flat field.

Instead, we treat this variability by removing a linear function of position from the computed photometry at each of the fourteen dither positions. Fitting functions with a higher-order dependence on position, or including cross terms, does not change our final results and increases the Bayesian Information Criterion ($\text{BIC} = \chi^2 + k \ln N$, where k is the number of free parameters and N is the number of points). We remove the systematic effects, and assess possible phase functions, by fitting the j^{th} data point at the i^{th} dither position (f_{ij})

with the following equation:

$$f_{ij} = (a + b \sin [\Omega_{\text{orb}} t - \Phi_0]) (1 + c_i + d_i x_{ij} + e_i y_{ij}) \quad (1)$$

This equation contains three astrophysical parameters and 42 instrumental parameters that account for the nonuniform detector response. The astrophysical parameters of interest are the average system flux a and a time (t)-dependent sinusoidal phase function with known planetary orbital frequency Ω_{orb} but unknown amplitude b and phase offset Φ_0 . The remaining parameters represent systematic effects to be removed: residual sensitivity corrections c_i and linear dependence on detector position (d_i, e_i) for each of the fourteen time series.

To prevent parameters a and b from floating we artificially set c_1 to satisfy the relation $\Pi_i (1 + c_i) = 1$. Ignoring the (d_i, e_i) factors does not change our final result for the 2009 dataset but increases the BIC, indicating a poorer fit to the data. For the purposes of backwards comparison, we also apply our analysis to the observations of H06. Due to the limited temporal coverage of this dataset including the (d_i, e_i) does not improve the fit; therefore we use only 17 parameters when reanalyzing this earlier dataset. We otherwise apply the same data reduction steps as described above.

In this work we consider only a sinusoidal phase function. Although we recognize that the phase curve will not be truly sinusoidal in shape, such a model is simple to work with and has a straightforward interpretation as a two-hemisphere “orange slice” model (Cowan et al. 2007; Cowan & Agol 2008, see also Sec. 3.2 below). Since the motion-correlated flux variation only depends on relative motion (rather than on absolute detector position) we normalized the (x_{ij}, y_{ij}) in Eq. (1) by subtracting the mean position in each of the fourteen time series.

2.4. Calibration and instrument stability

Our continuous photometry reveals that the MIPS background flux changes discontinuously from one AOR to the next. Stellar photometry is not similarly affected. The background flux varies at the level of 0.1%, comparable in amplitude to the expected planetary signal. We also see these discontinuities in background flux during MIPS observations of HD 189733b (Knutson et al. 2009) and HD 209458b (unpublished; Spitzer Program ID 40280).

Because the measured background level varies with the Spitzer AORs it is extremely unlikely that this variability is of astrophysical origin. It is also unlikely that the background variability results from the calibration process because we see the same effect in both the raw and calibrated data products. We observe no correlation between the background variability and the various reported instrumental parameters, though we cannot rule out either intermittent scatter from other sources or slight changes in the detector bias. A global sensitivity drift does not seem to be the culprit because the changes in background flux are uncorrelated with stellar photometry.

Although we were unable to determine the cause of the background variations, we suspect that they are due to small changes in the amount of scattered light reaching the MIPS detector. Variable scattered light could also explain our inability to remove the motion-correlated photometric jitter with an empirical flat field. Stel-

⁹ Generated using Tiny Tim; available at <http://ssc.spitzer.caltech.edu/>

lar photometry was substantially more stable on short timescales than was the background in all of the extended MIPS $24\mu\text{m}$ observations we examined, so we use this photometry in our subsequent analysis.

Our observations include a flux calibrator star to check MIPS’s long-term photometric stability. MIPS $24\mu\text{m}$ photometry is known to be stable at the 0.4% level over several years (Engelbracht et al. 2007); if it were this variable on short timescales we would be unable to discern the expected planetary emission. We observed the K1 III star HD 9712, taken from a catalog of bright interferometric calibrator stars (Mérand et al. 2005), during six AORs. In our reduction of these data we do not apply a correction for pixel motions and we achieve a repeatability of $\sim 10^{-4}$. These observations, shown as the red triangles in Figure 3, imply that the MIPS $24\mu\text{m}$ detector was stable over the course of our observations, and so we rule out detector sensitivity drifts as the source of the observed flux variations.

The level of MIPS photometric stability was not well known early in the Spitzer mission, so H06 used the background, attributed to smoothly-varying zodiacal emission, as a calibrator to adjust the photometry (see H06 Figure 1B). As we now suspect the MIPS background variations to result from scattered light in the instrument, there is no longer any need, nor possibility, to use the zodiacal light as a calibrator. The H06 data were part of a preliminary Spitzer program to assess variability of several systems for subsequent study in programs such as ours. Its five ν And AORs were taken at separate epochs and there was no calibrator star, so it was impossible to make the assessment described above. We have reanalyzed the H06 data using our new procedure and find values consistent with those plotted in H06 Figure 1A (see our Figure 3) and also with our new data. Thus, H06 did still present the first orbital phase variation for an exoplanet. The phase curve fit here to the H06 data provides accurate parameters for that dataset.

3. RESULTS

3.1. System flux

Although our primary science result – the planetary phase curve described below – is inherently a relative measurement, our observations also allow us to measure precise, absolute $24\mu\text{m}$ photometry for the ν And system. We measure $F_\nu = 0.488$ Jy and 0.490 Jy for the 2009 and 2006 datasets, respectively. These fluxes differ by 0.4%, which is at the limit of the MIPS $24\mu\text{m}$ precision; we therefore report the mean system flux as 0.489 ± 0.002 Jy. This value is significantly discrepant from the IRAS $25\mu\text{m}$ flux of 0.73 ± 0.05 Jy (Moshir 1989), but it is consistent with a Kurucz (1979) stellar spectrum tied to optical and near-infrared photometry of ν And from the Tycho-2 (Høg et al. 2000) and 2MASS (Skrutskie et al. 2006) catalogs.

3.2. A two-hemisphere model

As shown in Figure 3 and discussed below, we detect a flux variation consistent with the orbital period of ν And b. This measurement allows us to put tight constraints on the temperature contrast and phase offset of the planet. We interpret the observed flux variation in the context of a planet composed of two blackbody

hemispheres of constant temperature – i.e., a two-wedge “orange slice” model (c.f. Cowan et al. 2007). Sufficiently precise observations of such a bifurcated planet will reveal a flux variation with peak-to-trough amplitude

$$\frac{\Delta F_P}{\langle F \rangle} = \frac{B_\nu(T_{P1}) - B_\nu(T_{P2})}{B_\nu(\gamma T_{\text{eff}})} \left(\frac{R_P}{R_*} \right)^2 \sin i, \quad (2)$$

which normalizes the full amplitude of the planetary flux variation ΔF_P by the mean flux from the system $\langle F \rangle$; in Eq. (1) $\Delta F_P / \langle F \rangle = 2b/a$. The quantity γ accounts for the star being fainter in the mid-infrared than a blackbody with temperature T_{eff} ; at $24\mu\text{m}$ we set $\gamma = 0.8$ based on the models of Kurucz (1979). Thus, measuring $\Delta F_P / \langle F \rangle$ gives the hemispheres’ brightness temperature contrast relative to the stellar flux, modulo a $\sin i$ ambiguity. By assuming a planetary albedo A_B and assuming all emitted radiation is reprocessed starlight, a second (bolometric) relation obtains:

$$(1 - A_B) \frac{R_*^2}{2a^2} T_{\text{eff}}^4 = T_{P1}^4 + T_{P2}^4. \quad (3)$$

Thus, we implicitly assume that each hemisphere of our model planet emits a bolometric flux equal to that of a blackbody with the $24\mu\text{m}$ brightness temperature in Eq. (2). Subject to this assumption and given known or assumed values for the albedo A_B and planetary radius R_P , one can use Eqs. (2) and (3) to determine the hemispheric temperatures T_{P1} and T_{P2} at arbitrary orbital inclinations.

Setting $T_{P2} = 0$ and $T_{P1} = T_{P1,\text{max}}$ gives the minimum planetary radius capable of reproducing the observed flux variation, $\Delta F_P / \langle F \rangle$, as a function of the orbital inclination. Because this relation depends on inclination as $(\sin i)^{-1/2}$, measuring $\Delta F_P / \langle F \rangle$ gives an upper limit to the planet’s surface gravity:

$$g \leq \frac{G(m \sin i)}{R_*^2} \frac{B_\nu(T_{P1,\text{max}})}{B_\nu(\gamma T_{\text{eff}})} \left(\frac{\Delta F_P}{\langle F \rangle} \right)^{-1}. \quad (4)$$

3.3. Model fits

We determine the best-fit parameters using Powell’s (1964) method for multivariate minimization (the SciPy function `optimize.fmin_powell`), and assess their uncertainties and correlations with a Metropolis-Hastings, Markov-chain Monte Carlo analysis (MCMC; see Press et al. 2007, section 15.8). Table 1 (for the 2009 data) and Table 2 (for the 2006 data) report these results. Table 3 lists the astrophysical parameters of interest. We list the χ^2 and BIC values for the fits in Table 4. Parameter uncertainties are estimated from distributions generated using the kernel density method (KDE, implemented using the SciPy function `stats.gaussian_kde`) by determining the parameter values with equal KDE frequency that enclose 68% of the distribution.

MCMC analysis evolves an initial set of parameters in a way that is ultimately representative of their underlying probability distributions. For our Markov chain we choose a step size to give approximately a 30% step acceptance rate. To adequately sample the full parameter space we found it necessary to run the Markov chains longer for the 2006 dataset than for the 2009 dataset.

For the 2009 dataset we first ran the chain for 10^6 burn-in steps and discarded these; we then ran the chain for 2×10^7 steps, saving every 1000th step. For the 2006 dataset our procedure is the same but the burn-in phase lasted for 10^7 steps and the chain was then run for 5×10^7 steps, saving every 1000th step. We inspected correlation plots for all possible parameter pairs in both analyses to ensure adequate coverage of phase space and to assess parameter correlations.

All the one-dimensional parameter distributions are unimodal and approximately Gaussian in shape. We see some correlations between the d_i and e_i , which is unsurprising given the degree of correlation between the X and Y components of motion as shown in the middle panels of Figure 1. More surprising is a correlation between the mean system flux, a , and the phase offset, Φ_0 , as shown in Figure 4. Using a simulated dataset with white noise, we confirmed that when forcing a fit to a sinusoid of known period, a slightly higher mean value be counteracted by a slightly lower phase offset; however, we observe the opposite correlation. In any case no significant correlation is apparent between the phase curve amplitude $\Delta F_P/\langle F \rangle$ and the phase offset, which are the primary quantities of interest for our analysis. The best χ^2 from the MCMC is consistent to within a small fraction of the uncertainties with the optimizer values.

The model in Eq. (1) provides a good fit to both the astrophysical flux modulation and the instrumental flux variations at each of the fourteen dither positions, as shown in Figure 2. We plot the photometry after removal of the systematic effects in Figure 3, along with the best-fitting sinusoidal phase curve, for both the 2006 and 2009 datasets. Both datasets appear to vary approximately in phase; this coherence is a strong argument that the flux modulation we see is due to the planet v And b. The goodness-of-fit statistics (χ^2 and BIC) for both datasets are listed in Table 4. The high χ^2 for the 2009 dataset probably results from a somewhat non-sinusoidal phase curve and from the residual systematics apparent in Figure 3.

3.4. Phase curve amplitude

We measure values of $\Delta F_P/\langle F \rangle$ of $\Delta F_P/\langle F \rangle = 0.001300 \pm 0.000074$ for the 2009 data and 0.00090 ± 0.00022 for our reanalysis of the 2006 data, as shown in Table 3. Using the absolute calibration from Sec. 3.1, we find absolute peak-to-trough phase curve amplitudes of 0.636 ± 0.036 mJy and 0.44 ± 0.11 mJy for the 2009 and 2006 datasets, respectively. Thus the detection of the phase curve amplitude at both epochs is statistically significant at the $> 4\sigma$ level and is substantially smaller than reported by H06 (due to the calibration issues discussed above). The two epochs' phase curve amplitudes are consistent at the 1.7σ level; thus there is no evidence that the planetary emission exhibits inter-epoch variability. The lack of variability is consistent with the recent results of Agol et al. (2010), who set an upper limit of 2.7% on HD 189733b's dayside flux variations.

As v And b's orbit is inclined toward face-on, a greater intrinsic temperature contrast is required to generate the observed flux variation. Using Eq. (2) and our measurement of the phase curve amplitude we determine the expected day/night contrast ratio and plot it in the up-

per panel of Figure 5. We also plot the upper limits on the day/night contrast assuming planetary radii of 1.3 (1.8) R_J ; the implication is that the planet's orbital inclination angle is likely $\gtrsim 28^\circ$ (14°). These limits complement the preliminary limits on v And b's orbital inclination from the stability modeling of McArthur et al. (2010), which suggest $i \sim 20^\circ - 45^\circ$.

Invoking Eq. (3) allows us to determine the brightness temperatures of the planetary hemispheres in our model at each inclination angle. We assume zero albedo (c.f. Rowe et al. 2008) and a planetary radius of 1.3 R_J and plot the hemispheres' temperatures and 3σ limits in the lower panel of Figure 5. This sets a lower bound to the temperature contrast between the two hemispheres to be $T_{P1} - T_{P2} \gtrsim 900$ K. The hotter hemisphere's temperature remains in the range ~ 1700 -1900 K as we vary the radius from 1.0 R_J to 1.8 R_J ; however larger radii result in higher temperatures for the cooler hemisphere to maintain the measured flux and thus decrease the temperature contrast.

Using Eq. (4) we find that v And b's surface gravity is < 2100 cm s⁻² with 3σ confidence: this result is independent of assumptions about the planet's radius or orbital inclination. For a hot hemisphere temperature of ~ 1800 K (c.f. Figure 5) this limit on the surface gravity implies an atmospheric scale height > 300 km. In Figure 6 we plot the allowed regions of mass-radius parameter space against the known population of transiting extrasolar planets. Thus, our measurements suggest that v And b has a lower surface gravity than Jupiter, HD 189733b, and a number of other transiting extrasolar planets. This result demonstrates that v And b is indeed a gaseous Jovian planet, but we cannot determine whether it is a highly inflated planet or whether it is dominated by a sizeable rocky core.

3.5. Phase offset

Because v And b does not transit its host star we know its orbital ephemeris less precisely than we do for transiting planets. We used the Systemic Console¹⁰ (Meschiari et al. 2009) to reanalyze the published radial velocity data of v And (Butler et al. 1997; Naef et al. 2004; Butler et al. 2006; Wittenmyer et al. 2007; McArthur et al. 2010) using Systemic's Levenberg-Marquardt algorithm and ignoring system stability constraints. We obtain orbital parameters consistent with those of McArthur et al. (2010). By providing the covariances between the various fit parameters, this reanalysis allows a substantially more precise estimate of the planetary ephemeris than is available from the literature. We compute a time of zero relative radial velocity (phase 0.5, or secondary eclipse in a circular transiting system) of $\text{JD} = 2\,454\,868.78 \pm 0.07$ (1σ), which corresponds to an uncertainty of $\sim 6^\circ$ in determining the phase offset.

Assuming a two-hemisphere model, we find a phase offset of $84.5^\circ \pm 2.3^\circ$ relative to the computed ephemeris. This uncertainty may be an underestimate since we artificially constrain our phase curve to be sinusoidal. Knutson et al. (2009) discuss the artificially low uncertainties obtained from fitting to an arbitrarily chosen model, though here we have substantially broader phase coverage than was available in that study. The system flux

¹⁰ available from <http://oklo.org/downloadable-console/>

reaches a maximum before phase 0.5, indicating that the brighter hemisphere is offset to the east of the substellar point, as observed for HD 189733b (Knutson et al. 2007, 2009; Agol et al. 2010).

This large phase offset is strikingly different from the near-zero phase offset reported by H06; this difference is due to the choice of system calibration as discussed above. From our reanalysis of the 2006 data we find a phase offset of $57^\circ \pm 21^\circ$ relative to our ephemeris. The phase offsets at the two epochs are consistent at the 1.3σ level, and thus there is no evidence for inter-epoch variability in the phase offset.

4. DISCUSSION

The most striking result of our analysis is the large phase offset evident in the light curve. The direction of the phase offset is broadly consistent with the prediction by many circulation models of a large-scale, high-velocity, eastward-flowing jet on hot Jupiters (Cho et al. 2003; Cooper & Showman 2005; Cho et al. 2008; Showman et al. 2009; Burrows et al. 2010; Rauscher & Menou 2010; Thrastarson & Cho 2010) and as seen on HD 189733b (Knutson et al. 2007, 2009). However, the magnitude of the phase offset is far larger than is predicted at the low pressures characteristic of the $24\ \mu\text{m}$ photosphere (Showman et al. 2009).

A partial explanation for such a large phase offset could be that v And b’s atmosphere is substantially transparent to the incident stellar flux, with the result that the insolation is deposited at sufficient depth for substantial advection to occur. In this case, the planet might lack an atmospheric temperature inversion. Indeed, the large phase offset is more consistent with expectations for a planet lacking a temperature inversion than with expectations for a planet with an inverted atmosphere (c.f. HD 189733b vs. HD 209458b; Showman et al. 2009). Cooper & Showman (2005, 2006) predicted maximum hemisphere-averaged temperatures to be offset by $\gtrsim 60^\circ$ for an irradiated planet with no high-altitude absorbers, but it is unlikely that this would translate into high phase offsets at $24\ \mu\text{m}$ due to the high altitude of the photosphere at this wavelength. The absence of a temperature inversion is at odds with the recent proposal by Knutson et al. (2010) that, due to the lack of activity apparent in optical spectra of v And one would expect v And b to have a temperature inversion. Thrastarson & Cho (2010) also show clear shifted hot regions at higher pressure; the deep vortices produced by their simulations are several hundreds of degrees hotter than the surroundings.

Setting aside the phase offset for a moment, the phase curve amplitude we measure could be directly interpreted in the context of the models of Showman et al. (2009) as a typical phase curve for a planet with orbital inclination of 50° - 60° . However, simulations with greater phase offsets tend to show lower phase curve amplitudes (e.g. Showman et al. 2009; Burrows et al. 2010); thus it is difficult to simultaneously explain both amplitude and offset and it is difficult to reconcile current theory with our observations.

Alternatively, the large phase offset we see could represent reradiation of thermal energy deposited in shock fronts in the planet’s atmosphere. Many simulations predict supersonic equatorial jets on hot Jupiters that carry substantial kinetic energy; shocks could manifest

themselves where the jet transitions to subsonic speeds. Rauscher & Menou (2010) note that their simulations, as well as those of Showman et al. (2009), exhibit structures which could be interpreted as shocks – however, these models do not explicitly treat shock physics. Dobbs-Dixon et al. (2010) observe similar features in their models using an additional artificial viscosity factor to simulate shock behavior, and note that in high-altitude, high-velocity regions the energy carried by kinetic energy becomes comparable to the enthalpic energy. Watkins & Cho (2010) have recently suggested that gravity waves in the atmosphere of a hot Jupiter can also heat the planet’s upper atmosphere. It is unclear whether either shocks or gravity waves can deposit sufficient energy in the $24\ \mu\text{m}$ photosphere to cause the large phase offset we see. We look forward to further research into these topics to determine whether these or other phenomena can explain our observations.

We must also consider the possibility that the periodic flux modulation we see is intrinsic to the star rather than emanating from the planet. Shkolnik et al. (2005, 2008) report evidence for intermittently periodic stellar activity in this system correlated with v And b’s orbital period. They interpret this periodicity as a possible magnetospheric star-planet interaction, but they detect this periodicity at only some of their observational epochs. The consistency between our analysis of the 2006 and 2009 MIPS data suggests we are not seeing such a transient phenomenon, although analysis of additional activity measurements (e.g., from the Keck Observatory Archive) spanning the time of our Spitzer observations would help solidify this claim. Shkolnik et al. (2005) also report variations consistent with zero phase offset, which disagree with our observed phase offset. In addition, $24\ \mu\text{m}$ stellar variability at the level we observe would imply much greater variability at optical wavelengths: this is not observed (Henry et al. 2000). Finally, as discussed by H06, energy considerations indicate that such an intense star-planet interaction would cause the planet to spiral into the star in $\lesssim 10^7$ yr. Thus, the $24\ \mu\text{m}$ flux variations are likely to be of planetary origin.

Although a general framework exists within which to interpret observations of exoplanetary atmospheres, our understanding is still extremely limited. Madhusudhan & Seager (2009) demonstrate that some planets with claimed inversions can also be fit by non-inverted atmospheric models due to much greater number of free model parameters versus the limited number of observational constraints. In addition, there may be reason to question the reliability of some of the circulation models currently in use. Thrastarson & Cho (2010), in their extensive exploration of initial condition parameter space, have recently shown the extreme susceptibility of at least one circulation model to minute variations in initial conditions, resulting in substantial variability in final “steady-state” temperature contrasts and phase offsets. This chaotic behavior calls into question the ability of at least some models to make accurate, qualitative predictions about any of the quantities we are interested in. Other models (e.g., Dobbs-Dixon et al. 2010) exclude planets’ polar regions from their simulations, where large vortices are often seen to form (Cho et al. 2003, 2008; Rauscher et al. 2008). While the polar regions present a small cross-sectional area in transiting

systems, for non-transiting systems such as v And b polar emission will constitute a larger component of the observed system flux. A fully consistent three-dimensional circulation geometry is essential for comparison to our observations. Nevertheless, it is important to remember that general circulation models have trouble predicting global weather patterns even for relatively well-studied solar system planets; thus, a comprehensive, quantitative understanding of extrasolar planetary atmospheric dynamics will likely remain elusive for some time to come.

5. CONCLUSIONS AND FUTURE WORK

We have described a new $24\ \mu\text{m}$ phase curve, which we interpret as being due to emission from the planet v Andromedae b modulated by the planet’s orbit. Using a simple two-hemisphere model we determine the peak-to-trough phase curve amplitude to be 0.001300 ± 0.000074 . This result suggests an average “hot side” temperature of ~ 1800 K; for an average-sized hot Jupiter ($1.3 R_J$) this implies a hemisphere-averaged planetary temperature contrast of ~ 900 K and an orbital inclination $i \gtrsim 28^\circ$.

We find a phase offset of $84^\circ \pm 2^\circ \pm 6^\circ$, where we break the uncertainty into the error relative to our ephemeris and the error in our ephemeris, respectively. Such a large phase offset is difficult to reconcile with most current models. The phase curve is hotter hemisphere is offset to the east, as previously observed for HD 189733b (Knutson et al. 2007, 2009).

We reanalyze our earlier (H06) observations of this system and find a phase curve amplitude of 0.00090 ± 0.00022 and a phase offset of $57^\circ \pm 21^\circ \pm 6^\circ$. There is no evidence for inter-epoch variability in the planetary phase curve. This is primarily due to the large uncertainties from the 2006 dataset and demonstrates the difficulty in measuring such variability with sparsely-sampled phase curves.

There are substantial challenges in interpreting a phase curve observed at only a single wavelength due to the degeneracies between planetary radius, orbital inclination, and atmospheric composition and structure (Burrows et al. 2008). Some of these difficulties could be mitigated with phase curve measurements at additional wavelengths – ideally from space (i.e., warm Spitzer) but also potentially from ground-based near-infrared observations (e.g., Barnes et al. 2010). For example, commensurate phase curve amplitudes at both $3.6\ \mu\text{m}$ and $4.5\ \mu\text{m}$ would suggest that v And b does indeed lack a temperature inversion. On the other hand, differing phase curve amplitudes at these wavelengths could suggest an inversion and be more difficult to reconcile with the large phase offset at $24\ \mu\text{m}$. Phase offsets in these or other scenarios would also depend on the particular atmospheric temperature structure of the planet. Phase curves at $24\ \mu\text{m}$ currently exist for only two planets, v And b and HD 189733b (though unpublished data ex-

ist for HD 209458b). Cool, inversionless HD 189733b is probably the best-characterized extrasolar planet, and additional phase curves are already being observed for this object at $3.6\ \mu\text{m}$ and $4.5\ \mu\text{m}$. Phase curves of additional planets at multiple wavelengths are essential to ensure that our evolving views of the atmospheres of hot Jupiters are not biased by unbalanced datasets.

Whatever the cause of the substantial energy transport implied by the large phase offset we measure, if this phenomenon occurs in other (transiting) systems there are important implications for transmission spectroscopy. Line-of-sight effects cause optical transmission spectra to probe pressures comparable to those probed by mid-infrared emission; temperatures near the planetary terminator of ~ 1800 K (as we observe) should easily be detectable with ground- or space-based spectra. Sing et al. (2008) and Lecavelier des Etangs et al. (2008) infer a terminator temperature on HD 209458b of 2200 ± 260 K at 33 ± 5 mbar – roughly at the expected $24\ \mu\text{m}$ photosphere – which is not dissimilar from the hot terminator-centered hemisphere we observe on v And b. Further phase curve and transmission spectra of additional systems are needed to determine whether this hot, high-altitude terminator measurement results from a mechanism similar to what we observe on v And b.

We note that v And b is too bright to be observed photometrically at shorter wavelengths with the planned James Webb Space Telescope (though spectroscopy may be feasible). Given JWST’s magnitude limits and the expected high demand for its observing time, the community should consider a dedicated space-based mid-infrared photometry and spectroscopy mission (Vasisht et al. 2008). Such a mission would allow uninterrupted long-term monitoring of nearby hot Jupiter systems. This would provide high-precision measurements of these systems’ thermal emission and energy distributions, and possibly provide the first definitive evidence of dynamical meteorological processes – weather – on extrasolar planets.

We thank J. Colbert, C. Engelbracht, and G. Rieke for help in interpreting MIPS systematics, and T. Loredó for helpful discussions of statistics. This work is based in part on observations made with the Spitzer Space Telescope, which is operated by the Jet Propulsion Laboratory, California Institute of Technology under a contract with NASA. Support for this work was provided by NASA through an award issued by JPL/Caltech. We received free software and services from SciPy, Matplotlib, and the Python Programming Language. This research made use of Tiny Tim/Spitzer, developed by John Krist for the Spitzer Science Center; the Center is managed by the California Institute of Technology under a contract with NASA. Part of this work was performed while in residence at the Kavli Institute for Theoretical Physics, funded by the NSF through grant number PHY05-51164.

REFERENCES

- Agol, E., Cowan, N. B., Knutson, H. A., Deming, D., Steffen, J. H., Henry, G. W., & Charbonneau, D. 2010, ArXiv e-prints, ADS, 1007.4378
- Baines, E. K., McAlister, H. A., ten Brummelaar, T. A., Turner, N. H., Sturmman, J., Sturmman, L., Goldfinger, P. J., & Ridgway, S. T. 2008, ApJ, 680, 728, ADS, 0803.1411
- Barnes, J. R. et al. 2010, MNRAS, 401, 445, ADS, 0909.2510
- Burrows, A., Budaj, J., & Hubeny, I. 2008, ApJ, 678, 1436, ADS, 0709.4080
- Burrows, A., Rauscher, E., Spiegel, D., & Menou, K. 2010, ApJ submitted, ADS, 1005.0346
- Butler, R. P., Marcy, G. W., Williams, E., Hauser, H., & Shirts, P. 1997, ApJ, 474, L115+, ADS

- Butler, R. P. et al. 2006, ApJ, 646, 505, [ADS](#),
arXiv:astro-ph/0607493
- Charbonneau, D. et al. 2005, ApJ, 626, 523, [ADS](#),
arXiv:astro-ph/0503457
- Cho, J., Menou, K., Hansen, B. M. S., & Seager, S. 2003, ApJ, 587, L117, [ADS](#), arXiv:astro-ph/0209227
- , 2008, ApJ, 675, 817, [ADS](#), arXiv:astro-ph/0607338
- Cooper, C. S., & Showman, A. P. 2005, ApJ, 629, L45, [ADS](#),
arXiv:astro-ph/0502476
- , 2006, ApJ, 649, 1048, [ADS](#), arXiv:astro-ph/0602477
- Cowan, N. B., & Agol, E. 2008, ApJ, 678, L129, [ADS](#), 0803.3622
- Cowan, N. B., Agol, E., & Charbonneau, D. 2007, MNRAS, 379, 641, [ADS](#), 0705.1189
- Deming, D., Brown, T. M., Charbonneau, D., Harrington, J., & Richardson, L. J. 2005, ApJ, 622, 1149, [ADS](#),
arXiv:astro-ph/0412436
- Dobbs-Dixon, I., Cumming, A., & Lin, D. N. C. 2010, ApJ, 710, 1395, [ADS](#), 1001.0982
- Engelbracht, C. W. et al. 2007, PASP, 119, 994, [ADS](#), 0704.2195
- Ford, E. B., Rasio, F. A., & Sills, A. 1999, ApJ, 514, 411, [ADS](#),
arXiv:astro-ph/9807085
- Fortney, J. J., Lodders, K., Marley, M. S., & Freedman, R. S. 2008, ApJ, 678, 1419, [ADS](#), 0710.2558
- Fressin, F., Knutson, H. A., Charbonneau, D., O'Donovan, F. T., Burrows, A., Deming, D., Mandushev, G., & Spiegel, D. 2010, ApJ, 711, 374, [ADS](#), 0909.5221
- Fuhrmann, K., Pfeiffer, M. J., & Bernkopf, J. 1998, A&A, 336, 942, [ADS](#)
- Harrington, J., Hansen, B. M., Luszcz, S. H., Seager, S., Deming, D., Menou, K., Cho, J., & Richardson, L. J. 2006, Science, 314, 623, [ADS](#)
- Henry, G. W., Baliunas, S. L., Donahue, R. A., Fekel, F. C., & Soon, W. 2000, ApJ, 531, 415, [ADS](#)
- Høg, E. et al. 2000, A&A, 355, L27, [ADS](#)
- Knutson, H. A., Charbonneau, D., Allen, L. E., Burrows, A., & Megeath, S. T. 2008, ApJ, 673, 526, [ADS](#), 0709.3984
- Knutson, H. A. et al. 2007, Nature, 447, 183, [ADS](#), 0705.0993
- , 2009, ApJ, 690, 822, [ADS](#)
- Knutson, H. A., Howard, A. W., & Isaacson, H. 2010, ApJL submitted, [ADS](#), 1004.2702
- Kurucz, R. L. 1979, ApJS, 40, 1, [ADS](#)
- Lecavelier des Etangs, A., Vidal-Madjar, A., Désert, J., & Sing, D. 2008, A&A, 485, 865, [ADS](#), 0805.0595
- Madhusudhan, N., & Seager, S. 2009, ApJ, 707, 24, [ADS](#), 0910.1347
- Masci, F. J., Laher, R., Fang, F., Fowler, J. W., Lee, W., Stolovy, S., Padgett, D., & Moshir, M. 2005, in ASP Conference Series, Vol. 347, Astronomical Data Analysis Software and Systems XIV, ed. P. Shopbell, M. Britton, & R. Ebert, 468, [ADS](#)
- McArthur, B. E., Fritz, Benedict, G., Barnes, R., Martioli, E., Korzennik, S., Nelan, E., & Butler, R. P. 2010, ApJ, 715, 1203, [ADS](#)
- Mérand, A., Bordé, P., & Coudé du Foresto, V. 2005, A&A, 433, 1155, [ADS](#), arXiv:astro-ph/0412251
- Meschiari, S., Wolf, A. S., Rivera, E., Laughlin, G., Vogt, S., & Butler, P. 2009, PASP, 121, 1016, [ADS](#), 0907.1675
- Moshir, M. 1989, IRAS Faint Source Survey, Explanatory supplement version 1 and tape, ed. Moshir, M., [ADS](#)
- Naef, D., Mayor, M., Beuzit, J. L., Perrier, C., Queloz, D., Sivan, J. P., & Udry, S. 2004, A&A, 414, 351, [ADS](#),
arXiv:astro-ph/0310261
- Powell, M. J. D. 1964, The Computer Journal, 7, 155, [ADS](#)
- Press, W. H., Teukolsky, S. A., Vetterling, W. T., & Flannery, B. P. 2007, Numerical Recipes 3rd Edition : The Art of Scientific Computing, 3rd edn.
- Rauscher, E., & Menou, K. 2010, ApJ, 714, 1334, [ADS](#), 0907.2692
- Rauscher, E., Menou, K., Cho, J., Seager, S., & Hansen, B. M. S. 2008, ApJ, 681, 1646, [ADS](#), 0712.2242
- Reach, W. T. et al. 2005, PASP, 117, 978, [ADS](#),
arXiv:astro-ph/0507139
- Rieke, G. H. et al. 2004, in SPIE Conference Series, Vol. 5487, Optical, Infrared, and Millimeter Space Telescope, ed. J. C. Mather, 50–61, [ADS](#)
- Rowe, J. F. et al. 2008, ApJ, 689, 1345, [ADS](#), 0711.4111
- Santos, N. C., Israelian, G., & Mayor, M. 2004, A&A, 415, 1153, [ADS](#), arXiv:astro-ph/0311541
- Shkolnik, E., Bohlender, D. A., Walker, G. A. H., & Collier Cameron, A. 2008, ApJ, 676, 628, [ADS](#), 0712.0004
- Shkolnik, E., Walker, G. A. H., Bohlender, D. A., Gu, P., & Kürster, M. 2005, ApJ, 622, 1075, [ADS](#),
arXiv:astro-ph/0411655
- Showman, A. P., Fortney, J. J., Lian, Y., Marley, M. S., Freedman, R. S., Knutson, H. A., & Charbonneau, D. 2009, ApJ, 699, 564, [ADS](#), 0809.2089
- Sing, D. K., Vidal-Madjar, A., Lecavelier des Etangs, A., Désert, J., Ballester, G., & Ehrenreich, D. 2008, ApJ, 686, 667, [ADS](#), 0803.1054
- Skrutskie, M. F. et al. 2006, AJ, 131, 1163, [ADS](#)
- SSC. 2007, Spitzer Space Telescope Observer's Manual - Version 8.0, ed. Spitzer Science Center, California Institute of Technology, [ADS](#)
- , 2010, MIPS Instrument Handbook - Version 1.0, ed. Spitzer Science Center, California Institute of Technology, [ADS](#)
- Takeda, G., Ford, E. B., Sills, A., Rasio, F. A., Fischer, D. A., & Valenti, J. A. 2007, ApJS, 168, 297, [ADS](#),
arXiv:astro-ph/0607235
- Thrustarson, H. T., & Cho, J. 2010, ApJ, 716, 144, [ADS](#), 1004.2871
- Valenti, J. A., & Fischer, D. A. 2005, ApJS, 159, 141, [ADS](#)
- Vasisht, G., Swain, M. R., Akeson, R. L., Burrows, A., Deming, D., Grillmair, C. J., & Greene, T. P. 2008, in SPIE Conference Series, Vol. 7010, Space Telescopes and Instrumentation 2008, [ADS](#)
- Watkins, C., & Cho, J. Y.-K. 2010, ApJ, 714, 904, [ADS](#), 1003.4818
- Wittenmyer, R. A., Endl, M., & Cochran, W. D. 2007, ApJ, 654, 625, [ADS](#), arXiv:astro-ph/0609117

TABLE 1
PHASE CURVE AND CALIBRATION
PARAMETERS FROM EQ. (1) (2009 DATA)^a.

a^b	0.488436	±	0.000011 Jy
b	0.000317	±	0.000017 Jy
Φ_0^c	84.5°	±	2.3°
c_1	0.005367	±	0.000054
c_2	0.012926	±	0.000055
c_3	0.001180	±	0.000055
c_4	0.009498	±	0.000055
c_5	0.001548	±	0.000054
c_6	0.014334	±	0.000027
c_7	-0.006333	±	0.000054
c_8	-0.004193	±	0.000054
c_9	-0.002129	±	0.000054
c_{10}	-0.007009	±	0.000055
c_{11}	-0.000549	±	0.000055
c_{12}	-0.009458	±	0.000054
c_{13}	-0.002757	±	0.000054
c_{14}	-0.012002	±	0.000054
d_1	-0.00429	±	0.00072
d_2	0.00146	±	0.00070
d_3	-0.00214	±	0.00071
d_4	-0.00428	±	0.00070
d_5	-0.00520	±	0.00071
d_6	-0.00177	±	0.00070
d_7	-0.00100	±	0.00078
d_8	-0.00049	±	0.00072
d_9	0.00196	±	0.00066
d_{10}	-0.00252	±	0.00067
d_{11}	-0.00029	±	0.00066
d_{12}	-0.00409	±	0.00067
d_{13}	0.00259	±	0.00068
d_{14}	-0.00152	±	0.00068
e_1	0.00066	±	0.00080
e_2	0.00031	±	0.00079
e_3	0.00211	±	0.00040
e_4	0.00218	±	0.00078
e_5	0.00409	±	0.00080
e_6	0.00009	±	0.00080
e_7	0.00211	±	0.00081
e_8	-0.00259	±	0.00076
e_9	0.00628	±	0.00076
e_{10}	-0.00284	±	0.00039
e_{11}	-0.00168	±	0.00075
e_{12}	-0.0029	±	0.0011
e_{13}	-0.00061	±	0.00076
e_{14}	0.00025	±	0.00074

^a Errors quoted are the 68.3% confidence limits. The first three parameters are the mean system flux a , the phase curve half-amplitude b , and the phase offset Φ_0 . The other coefficients represent fits to the nonuniform detector response at each of the fourteen MIPS dither positions. The c_i are dimensionless, and the d_i and e_i are in units of pixel^{-1} .

^b The absolute accuracy of the mean system flux a is 0.4% as discussed by [Engelbracht et al. \(2007\)](#).

^c Φ_0 is measured relative to our computed ephemeris, as discussed in Sec. 3.5.

TABLE 2
PHASE CURVE AND CALIBRATION
PARAMETERS FROM EQ. (1) (2006
DATA)^a.

a^b	0.490250	±	0.000039 Jy
b	0.000221	±	0.000053 Jy
Φ_0^c	57°	±	21°
c_1	0.00284	±	0.00030
c_2	0.01423	±	0.00028
c_3	0.00112	±	0.00030
c_4	0.01094	±	0.00028
c_5	0.00235	±	0.00029
c_6	0.01574	±	0.00028
c_7	-0.00757	±	0.00027
c_8	-0.00596	±	0.00030
c_9	-0.00086	±	0.00030
c_{10}	-0.00755	±	0.00029
c_{11}	-0.00097	±	0.00029
c_{12}	-0.00945	±	0.00029
c_{13}	-0.00299	±	0.00027
c_{14}	-0.01138	±	0.00027

^a Errors quoted are the 68.3% confidence limits. The first three parameters are the mean system flux a , the phase curve half-amplitude b , and the phase offset Φ_0 . The other coefficients represent fits to the nonuniform detector response at each of the fourteen MIPS dither positions. The c_i are dimensionless, and the d_i and e_i are in units of pixel⁻¹.

^b The absolute accuracy of the mean system flux a is 0.4% as discussed by [Engelbracht et al. \(2007\)](#).

^c Φ_0 is measured relative to our computed ephemeris, as discussed in Sec. 3.5.

TABLE 3
ASTROPHYSICAL PARAMETERS OF INTEREST

	2006			2009		
$\Delta F/F$	0.00090	±	0.00022	0.001300	±	0.000074
Φ_0	57°	±	21°	84.5°	±	2.3°

TABLE 4
GOODNESS-OF-FIT STATISTICS

	2006	2009
χ^2	814.1	38422.7
k	17	45
N	838	23884
BIC	928.6	38876.4

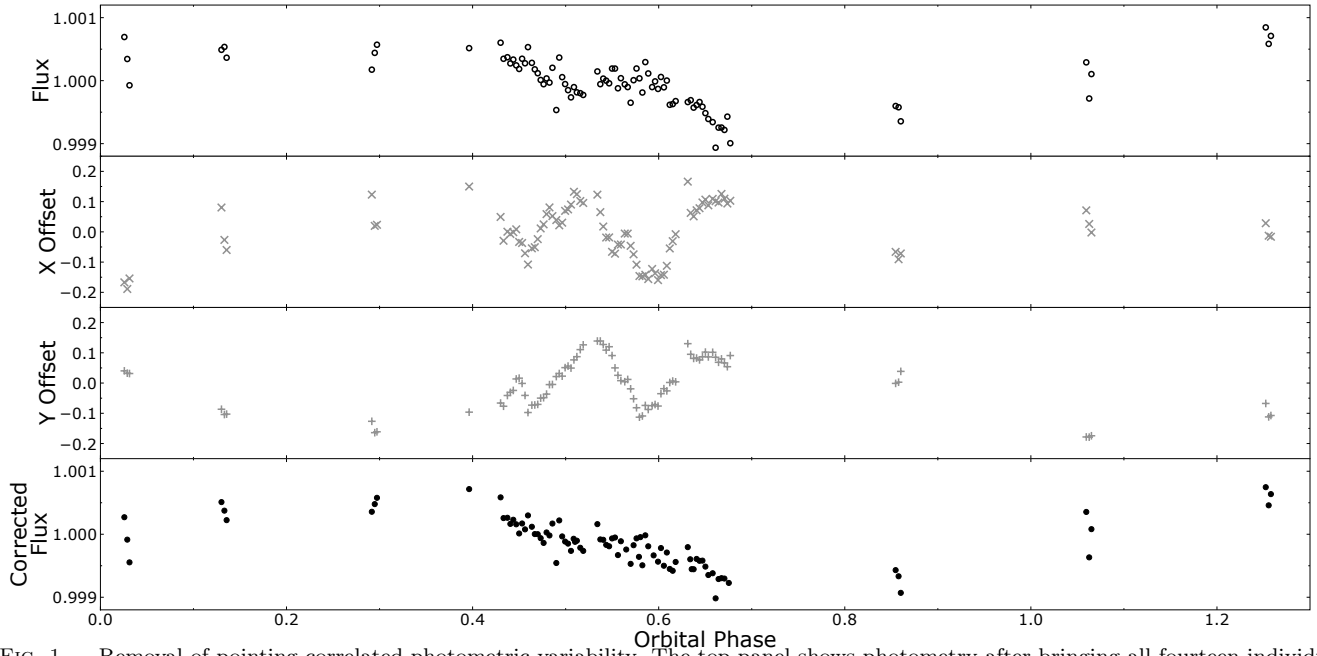


FIG. 1.— Removal of pointing-correlated photometric variability. The top panel shows photometry after bringing all fourteen individual time series to a common level. A large-scale sinusoidal flux variation is evident, but so is a shorter-scale “ripple” (near phase 0.5); this ripple is correlated with the motion of v And on the MIPS detector, plotted as X and Y in the middle two panels. The bottom plot shows the final, cleaned photometry after removing this correlation. For display purposes the full dataset has been averaged over each AOR in this figure. Uncertainties on the X and Y points are typically $\sim 10^{-3}$ pixel, while the uncertainties of the photometric points (not plotted for clarity) is typically $\sim 1.5 \times 10^{-4}$.

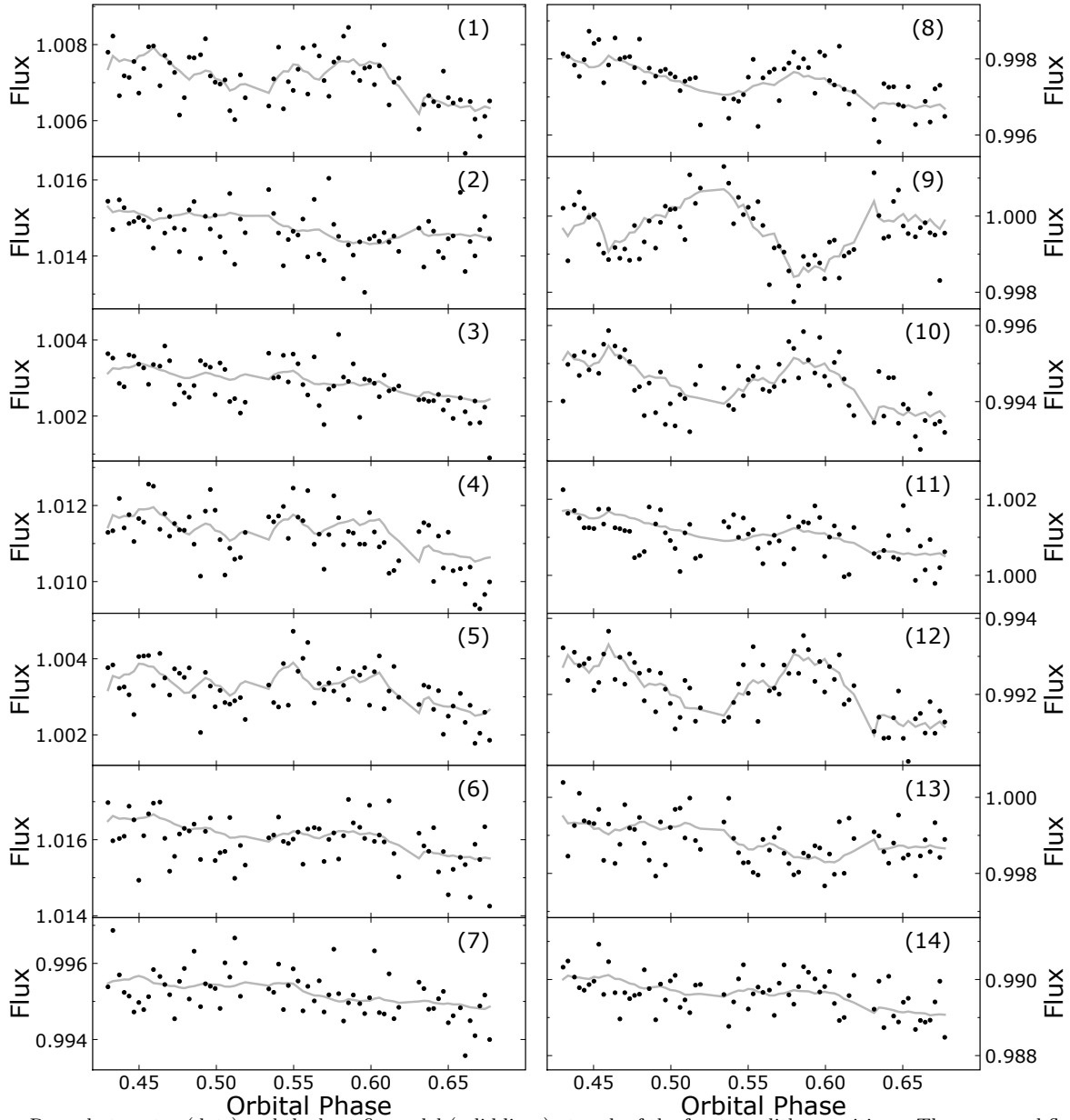


FIG. 2.— Raw photometry (dots) and the best-fit model (solid lines) at each of the fourteen dither positions. The measured flux varies by several percent from one position to another, as evidenced by the different scales in each panel. The downward trend evident in all panels is due to the decreasing flux from the system, shown more clearly in Figure 3. For display purposes the data have been averaged over each AOR and we plot only the continuous-observing segment of our observations. The precision of individual points (not plotted for clarity) is $\sim 5 \times 10^{-4}$.

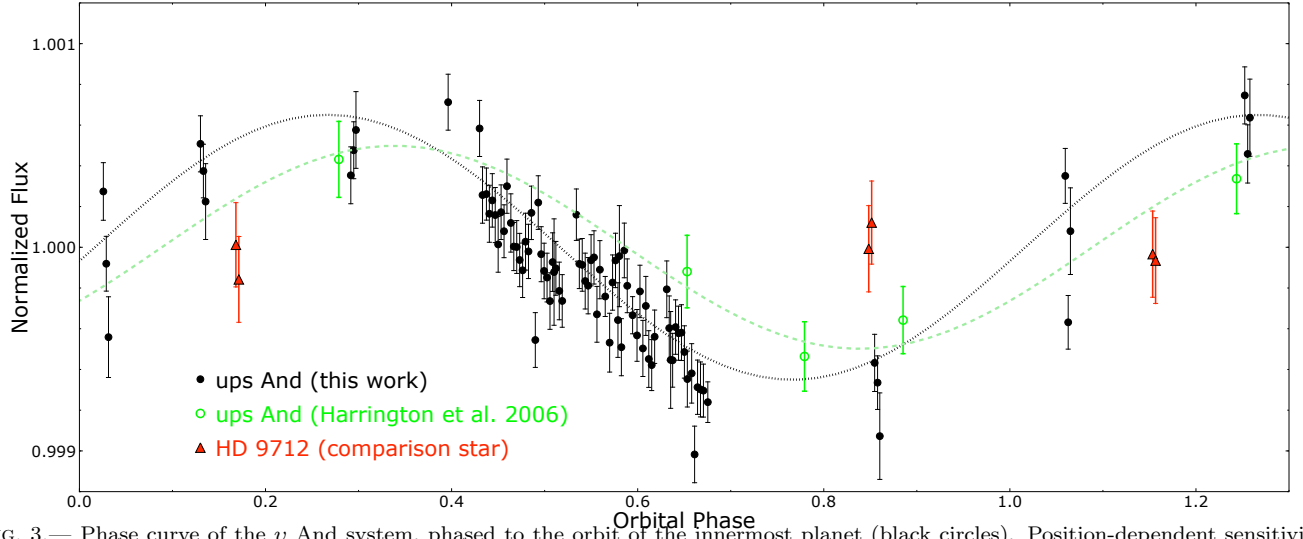


FIG. 3.— Phase curve of the v And system, phased to the orbit of the innermost planet (black circles). Position-dependent sensitivity effects have been removed and for display purposes we have averaged the data over each AOR. The best-fit sinusoid (black dotted line) exhibits a phase offset of $\sim 80^\circ$, consistent with a planetary “hot spot” advected almost to the planet’s day-night terminator. The light green circles are our reanalysis of the data from [Harrington et al. \(2006\)](#), and the light green dashed line shows the best-fit sinusoid to these data; the phase coherence between the 2006 and 2009 datasets is consistent with flux modulated by the innermost planet’s orbit. The red triangles show our flux calibrator observations, which are consistent with a constant detector sensitivity.

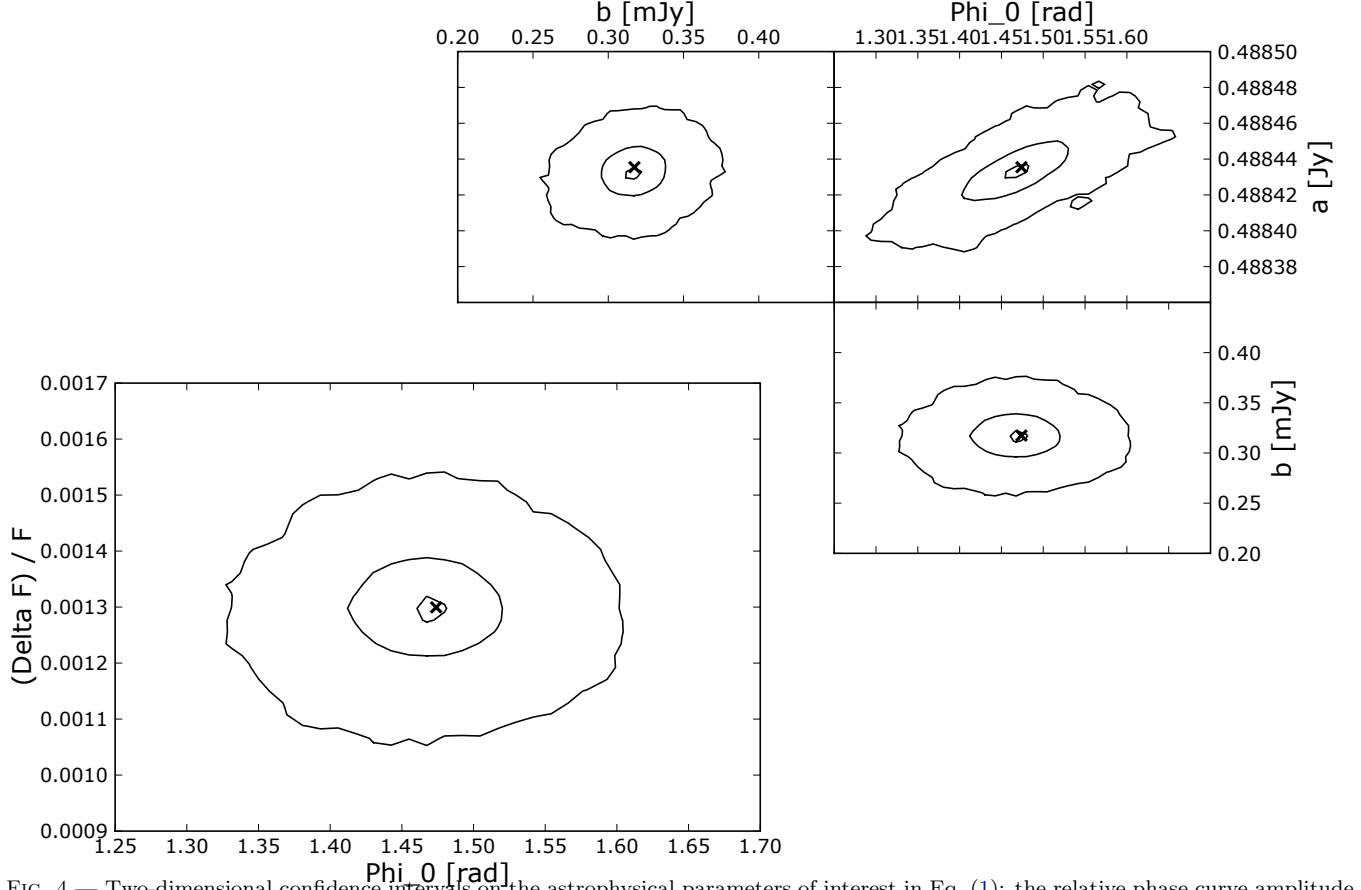


FIG. 4.— Two-dimensional confidence intervals on the astrophysical parameters of interest in Eq. (1): the relative phase curve amplitude $\Delta F_P/F$, the absolute mean system flux a , the phase curve half-amplitude b , and the phase offset Φ_0 . The solid lines are the contours that enclose 68.3%, 95.4%, and 99.7% of the parameter space from the 2009 dataset. The ‘x’ in each panel marks the best-fit parameter listed in Tables 1 and 3.

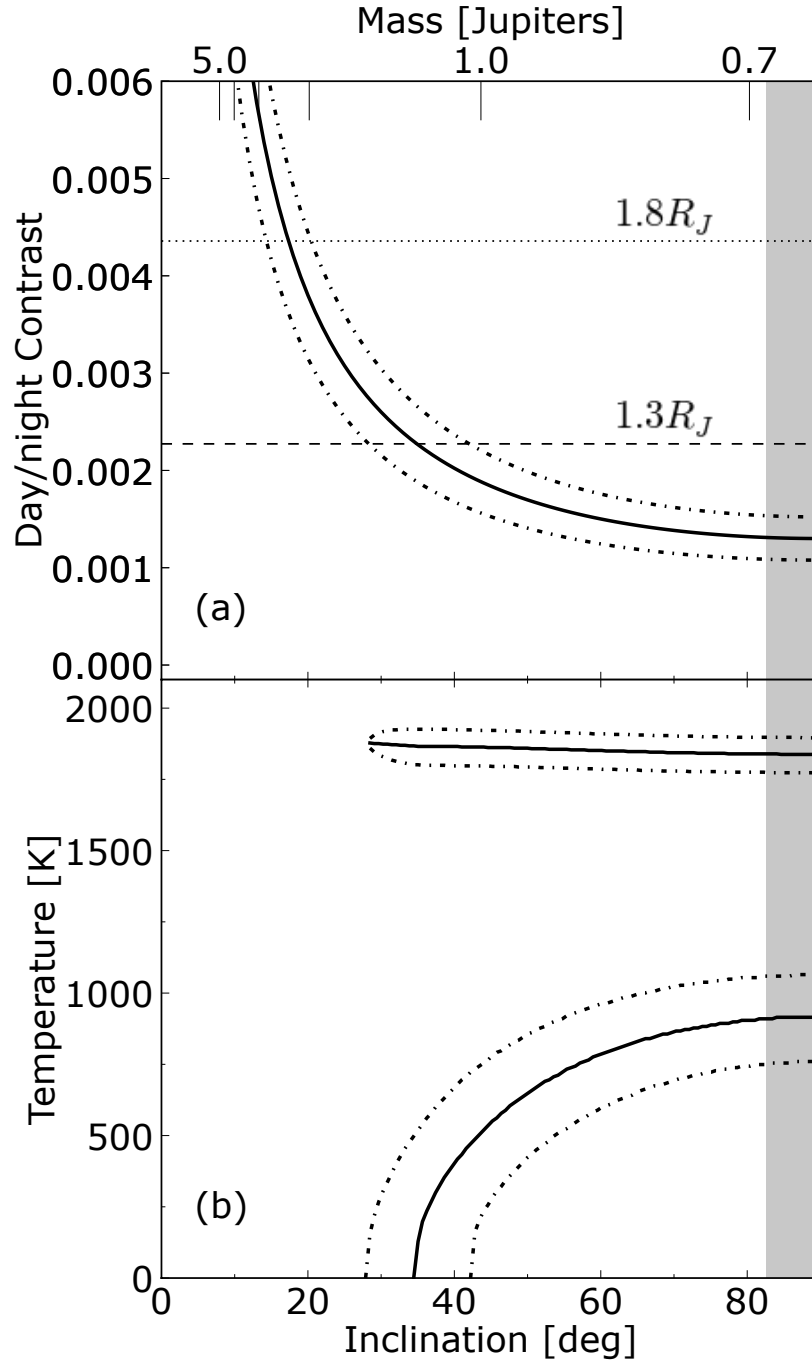


FIG. 5.— Day-night temperature contrast as a function of orbital inclination angle, assuming a planet with zero albedo. (a) Our measurement of the phase curve amplitude and Eq. (2) constrain the allowed day/night contrast to lie between the dot-dashed 3σ limits. The maximum allowable contrast for a planet of 1.3 (1.8) R_J is shown as the dashed (dotted) lines, suggesting a lower limit on the inclination angle of 25° (15°). (b) Considering Eq. (3) and assuming a radius of $1.3R_J$ allows us to determine the temperature of both hemispheres as a function of inclination (solid lines, with dot-dashed 3σ limits). This radius implies a planetary temperature contrast of $\gtrsim 900$ K. The cooler hemisphere is more sensitive to changes in planetary radius, though both temperatures increase as radius increases.

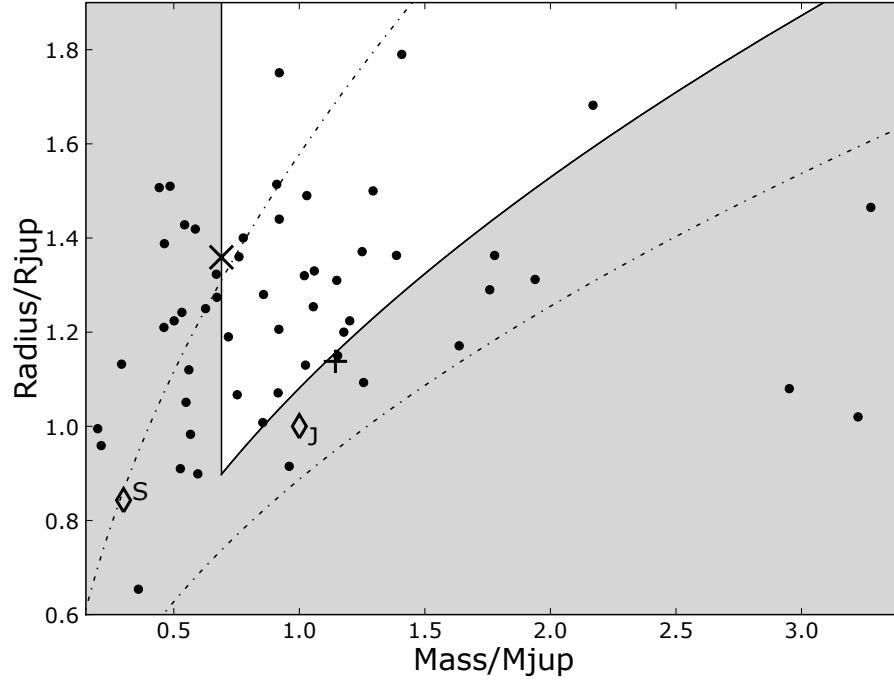


FIG. 6.— Mass/radius constraints for v And b from Eq. (4). The shaded area is the portion of mass-radius space excluded at the 3σ level. Points are known transiting extrasolar planets; measurement uncertainties have been omitted for clarity. Extrasolar planets that have been observed with MIPS are indicated by a ‘+’ (HD 189733b) and a ‘x’ (HD 209458b), while Jupiter and Saturn are marked with a ‘J’ and ‘S,’ respectively. The dot-dashed lines represent lines of constant surface gravity with $g = 10^3 \text{ cm s}^{-2}$ and $3.2 \times 10^3 \text{ cm s}^{-2}$. Our model and phase curve measurement constrain $g < 2100 \text{ cm s}^{-2}$ at the 3σ level.